Supplemental Material: Scalable Tight-Binding Model for Graphene

Ming-Hao Liu (劉明豪),[1] Peter Rickhaus,[2] Péter Makk,[2] Endre Tóvári,[3] Romain Maurand,[4]
Fedor Tkatschenko,[1] Markus Weiss,[2] Christian Schönenberger,[2] and Klaus Richter[1]

[1]*Institut für Theoretische Physik, Universität Regensburg, D-93040 Regensburg, Germany*
[2]*Department of Physics, University of Basel, Klingelbergstrasse 82, CH-4056 Basel, Switzerland*
[3]*Department of Physics, Budapest University of Technology and Economics and Condensed Matter Research Group of the Hungarian Academy of Sciences, Budafoki ut 8, 1111 Budapest, Hungary*
[4]*University Grenoble Alpes, CEA-INAC-SPSMS, F-38000 Grenoble, France*

(Dated: October 13, 2014)

Carrier density profile of the simulated device

As mentioned in the main text, the finite-element simulator FEniCS [1] together with the mesh generator GMSH [2] are adopted to compute the self-partial capacitances [3] of the individual metal contacts and bottom gates, $C_{\rm cL}, C_{\rm cR}, C_{\rm bogL}$, and $C_{\rm bogR}$, which are functions of two-dimensional coordinates (x,y). The classical contribution to the total carrier density $n(x,y)$ is given by the linear combination $\sum_{i=\rm cL,cR,bogL,bogR}(C_i/e)V_i$, where $V_{\rm bogL}$ and $V_{\rm bogR}$ are the left and right bottom gate voltages, respectively, and $V_{\rm cL}$ and $V_{\rm cR}$ are responsible for contact doping mainly arising from the charge transfer between the metal contacts and the graphene sheet. Since the experimental conditions are very similar to our previous work [4], we adopt the same empirical value of 0.04 V for both $V_{\rm cL}$ and $V_{\rm cR}$. Total carrier density follows Ref. 3. Two examples showing $n(x,y)$ profiles are given in Fig. S1, where zero intrinsic doping is assumed.

Carrier-energy relation in the presence of magnetic field

To compute the carrier density as a function of energy E and magnetic field B_z using the Green's function method, we consider an ideal graphene ribbon extending infinitely along the $\pm x$ axis. The retarded Green's function gives the total density of states of the supercell, $D(E,B_z) = -(1/\pi)\,\mathrm{Im}\,\mathrm{Tr}\,G^r(E,B_z)$, where we have explicitly denoted the dependence of the magnetic field B_z, which enters from the tight-binding Hamiltonian of the supercell. The carrier density in the zero temperature limit is given by integrating over the energy, $n(E,B_z) = (2/A)\int_0^E D(E',B_z)dE'$, where the factor 2 accounts for the spin degeneracy and $A = N(3\sqrt{3}a^2/4)$ is the area of the supercell with N the number of lattice sites within the supercell and $a = s_f a_0$ the lattice spacing.

An example for $n(E,B_z)$ using a scaled armchair graphene ribbon with $s_f = 4$ and $N_a = 101$ (about 100 nm wide) is given in Fig. S2(a). With the increasing B_z, the emergence of the relativistic Landau level spectrum is clearly seen, which is well described by

$$E_{n_L} = \mathrm{sgn}(n_L)E_1\sqrt{|n_L|} \quad , \quad E_1 = \sqrt{2eB_z\hbar v_F^2} \quad , \quad n_L = 0, \pm1, \pm2, \cdots . \tag{S1}$$

Thus properly scaled graphene also correctly captures the half integer quantum Hall physics of real graphene.

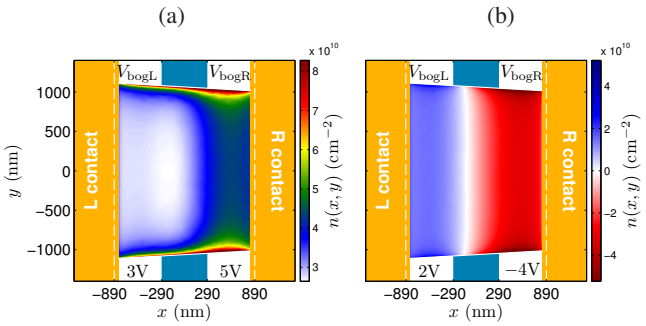

FIG. S1. Examples of carrier density profiles $n(x,y)$ with (a) unipolar and (b) bipolar gate voltage configurations. Bottom gate voltages are indicated in respective plots. The geometry follows the design values of the experiment, and the shape of the graphene flake is estimated from an optical image of the real device. The width of the bottom gates is 600 nm, and the white dashed lines indicate the edges of the bottom gates underneath the contacts.

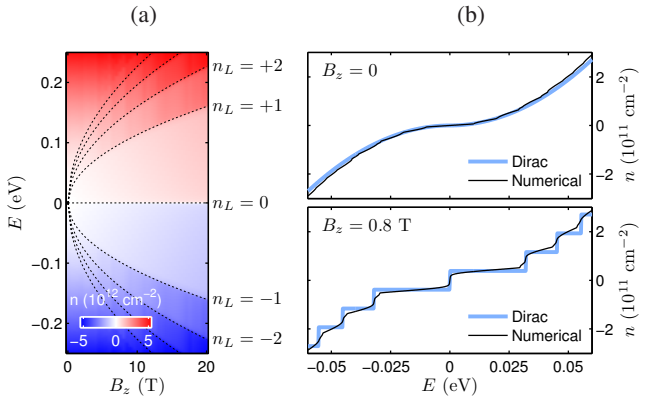

FIG. S2. (a) Carrier density as a function of energy E and magnetic field B_z, using an $s_f = 4, N_a = 101$ artificial armchair graphene ribbon (about 100 nm wide). The quantized carrier density is well described by the Landau level spectrum (dashed lines) given by Eq. (S1). (b) Carrier-energy relation at $B_z = 0$ (upper panel) and $B_z = 0.8$ T (lower panel), using an $s_f = 16, N_a = 50$ ribbon (about 200 nm wide). The numerical results are compared with the Dirac model, Eq. (S2) in the upper panel and Eq. (S3) in the lower panel.

In Fig. S2(b) we use another ribbon with $s_f = 16$ and $N_a = 50$ (about 200 nm wide) to compare the carrier-energy relation with and without magnetic field. For the $B_z = 0$ case [upper panel in Fig. S2(b)], despite the ribbon nature of the considered artificial graphene, the $n(E)$ relation is basically consistent with the Dirac model,

$$n_{\rm Dirac}(E) = {\rm sgn}(E)\frac{1}{\pi}\left(\frac{E}{\hbar v_F}\right)^2. \qquad \text{(S2)}$$

For the $B_z = 0.8\,$T case [lower panel in Fig. S2(b)], the numerical result exhibits quantized plateaus due to the emerging Landau levels. The plateaus are, however, not perfectly flat due to the level broadening of the density of states, which stems from the finite width of the considered ribbon, instead of temperature.

In the case of ideal infinite graphene, the density of states can be written as $D_{\rm Dirac}(E,B_z) = (4eB_z/h)\sum_{n_L}\delta(E-E_{n_L})$, where the prefactor accounts for the states each Landau level can accommodate and E_{n_L} is given in Eq. (S1). Integrating $D_{\rm Dirac}(E,B_z)$ with respect to energy, one obtains a perfectly quantized carrier-energy relation

$$n_{\rm Dirac}(E,B_z) = \frac{4eB_z}{h}\left({\rm sgn}(E)\left\lfloor\frac{E^2}{E_1^2}\right\rfloor + \frac{1}{2}\right), \qquad \text{(S3)}$$

where $\lfloor x\rfloor$ stands for the largest integer not greater than x (known as the floor function in computer science) and E_1 is given in Eq. (S1). Compared to the numerical $n(E,B_z)$ [lower panel in Fig. S2(b)], the ideal $n_{\rm Dirac}(E,B_z)$ given by Eq. (S3) is not suitable for describing the carrier-energy relation in finite-width graphene systems. Nevertheless, the formula confirms the correct trend of the numerical carrier-energy relation in the presence of magnetic field.

From the numerical $n(E)$ curve at a given B_z, such as that given in Fig. S2(b), the position of the highest filled energy level for a given carrier density, $E(n)$, is obtained, and the negative of it is the desired energy band offset for transport calculation, which is adopted in the simulations for Fig. 3(e) of the main text as well as the following unipolar quantum Hall regime.

Unipolar quantum Hall data

Figure S3(a) shows the measured unipolar conductance map $G(B_z,V_{\rm bog})$ with the two bottom gates connected together. By subtracting the contact resistance $R_c \approx 1080\,\Omega$, the quantized conductance at low field up to 0.2 T is compared with the computed transmission function using $s_f = 50$ scaled graphene in Fig. S3(b), in the presence of Anderson-type disorder with strength $U_{\rm dis} = 3\,$meV (see the main text). Note that the color range in Fig. S3(b) is adjusted to highlight the conductance plateaus up to filling factor $\nu = \pm 14$.

Despite the rather consistent Landau fan diagrams in both experiment and theory maps of Fig. S3(b), a closer look shows that the minimal B_z required to quantize the conductance in the experiment is larger than that in the simulation possibly because of thermal fluctuations not considered in the calculations. In addition, the slopes of the fan-shaped plateaus indicate a slightly different charging efficiency between the experiment and the simulation, which we analyze in the following.

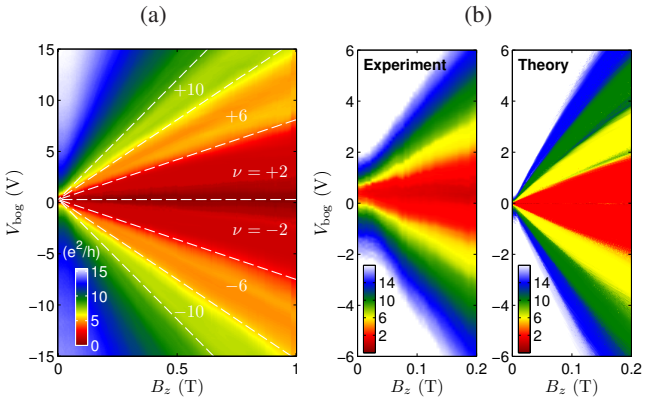

FIG. S3. (a) Experimental data of the conductance measured with the two bottom gates connected to each other ($V_{\rm bogL} = V_{\rm bogR} = V_{\rm bog}$) and magnetic field B_z sweep up to 1 T. The lowest 6 quantized conductance plateaus labeled by filling factors $\nu = \pm 2, \pm 6, \pm 10$ are separated by the fitting fan lines. (b) By subtracting the deduced contact resistance $R_c \approx 1080\,\Omega$, the experimental data at low field is compared with the theory data of the computed transmission function T.

Gate efficiency from the Landau fan diagram

The pronounced quantized conductance plateaus reported in Fig. S3(a) allows for a precise evaluation of the gate efficiency. Let the average gate capacitance of the connected bottom gates be $\bar{C}_g$ and assume a uniform chemical doping of concentration n_0. Relating the mean carrier density given by $\bar{n} = n_0 + \bar{C}_g V_{\rm bog}$ and filling factor $\nu = \bar{n}/(eB_z/h)$ one finds

$$V_{\rm bog} = \frac{e\nu}{\bar{C}_g h}B_z - \frac{n_0}{\bar{C}_g} \equiv c_1\nu B_z + c_2.$$

Thus on the measured field-gate map shown in Fig. S3(a), the slope of each fan line that separates two adjacent conductance plateaus $\nu - 2$ and $\nu + 2$ gives $c_1\nu = e\nu/\bar{C}_g h$ while the intersect at $B_z = 0$ gives $c_2 = -n_0/\bar{C}_g$. By fitting the experimental data at $\nu = 0, \pm 4, \cdots$, we find $c_1 = 1.95\,{\rm V\,T^{-1}}$ and $c_2 = 0.3\,$V, which yield a gate efficiency

$$\bar{C}_g = \frac{e}{c_1 h} = 1.24\times 10^{10}\,{\rm cm^{-2}\,V^{-1}}$$

and a weak chemical doping

$$n_0 = -c_2\bar{C}_g = -3.72\times 10^9\,{\rm cm^{-2}},$$

respectively.

Comments on speed-up and bilayer graphene

The strongly reduced memory demand brought by the scaling allows one to deal with previously prohibited micron-scale two-dimensional graphene systems. Even for computable systems, the speed-up can be seen in, e.g., the computation time Δt for the lead self-energy that typically grows with the cube of the number of lattice sites within the lead supercell, i.e., $\Delta t \to \Delta t/s_f^3$ after scaling. Taking the illustrated 2.2-micron-wide graphene for example, Δt is found to be $\sim 2.4\,\mathrm{s}$ on a single Intel Core i7 CPU for the artificial graphene scaled by $s_f = 100$. For $s_f = 1$, the time required to compute just a single shot of the self-energy, if the memory allowed, would be $\sim 2.4 \times (100)^3\,\mathrm{s}$, which is almost a month.

The scaling also applies to bilayer graphene, as clearly seen from its energy spectrum given by [5]

$$E(k) = \pm\sqrt{\frac{\gamma_1^2}{2} + \frac{U^2}{4} + \hbar^2 v_F^2 k^2 \pm \sqrt{\frac{\gamma_1^4}{4} + \hbar^2 v_F^2 k^2 \left(\gamma_1^2 + U^2\right)}}, \tag{S4}$$

with $\gamma_1 \approx 0.39\,\mathrm{eV}$ the interlayer nearest neighbor hopping and U the asymmetry parameter responsible for the gap. The appearance of the product ta in the dispersion (S4) after substituting $\hbar v_F = 3ta/2$ clearly suggests that the scaling condition [Eq. (1) of the main text] also applies to bilayer graphene with γ_1 and U left unaltered. Similar to the long wavelength limit [Eq. (2) of the main text] but due to the massive Dirac nature, the validity range of s_f is more limited than the single-layer case. In the case of gapless bilayer graphene, we have $s_f \ll 6\pi t_0/[(2|E_{\max}| + \gamma_1)^2 - \gamma_1^2]^{1/2}$, which suggests $s_f \ll 50$ for the single-band transport ($|E_{\max}| \leq \gamma_1$). In the presence of magnetic field, the restriction of Eq. (3) in the main text remains true.

[1] A. Logg, K.-A. Mardal, G. N. Wells, *et al.*, *Automated Solution of Differential Equations by the Finite Element Method* (Springer, 2012).

[2] C. Geuzaine and J.-F. Remacle, International Journal for Numerical Methods in Engineering **79**, 1309 (2009).

[3] M.-H. Liu, Phys. Rev. B **87**, 125427 (2013).

[4] P. Rickhaus, R. Maurand, M.-H. Liu, M. Weiss, K. Richter, and C. Schönenberger, Nature Communications **4**, 2342 (2013).

[5] E. McCann and M. Koshino, Reports on Progress in Physics **76**, 056503 (2013).